Robust hyperbolic plasmons in a graphene allotrope with dual anisotropic Dirac cones

Mingzheng Wang, Runyu Fan, Xikui Ma, Chao Ding, Lei Sun, Yangyang Li, and Mingwen Zhao*
School of Physics, Shandong University, Jinan 250100, China

(Received 16 November 2023; revised 25 July 2024; accepted 29 July 2024; published 8 August 2024)

Graphene has significantly influenced advanced photonics, due to its exceptional ability to confine light at atomic scales. However, the presence of isotropic Dirac cones (DCs) in graphene restricts its capability to support hyperbolic surface plasmon polaritons (SPPs) propagation without specific patterning treatments. Additionally, the plasmon frequency in graphene is highly sensitive to the Fermi level, making it unstable under external perturbations. In this study, we present a dual anisotropic Dirac cone (DADC) model that addresses these limitations. We demonstrate that this DADC exhibits highly in-plane anisotropic plasmons and extensive hyperbolic regions capable of supporting hyperbolic SPPs. By maintaining the Fermi level between the Dirac points of the two DCs, we ensure that the plasmon frequency remains independent of Fermi level. Furthermore, we identify ω-graphene, a graphene allotrope, as a potential material for this model. Our first-principles calculations revealed that ω-graphene exhibits significantly anisotropic plasmons, with a maximal frequency of 1.68 eV along the x direction and 0.128 eV along the y direction, accompanied by a low-loss hyperbolic region spanning from 0.48 to 1.16 eV. Notably, the plasmon frequency remains stable despite variations in Fermi energy within an experimentally attainable region. The highly directional propagation of SPPs in the hyperbolic regions was also confirmed using Maxwell's equations. These findings introduce a compelling candidate for SPPs devices and open exotic avenues for designing and investigating natural hyperbolic surfaces.

DOI: 10.1103/PhysRevB.110.085415

I. INTRODUCTION

To confine electromagnetic waves to atomic scales [1–3], highly localized plasmon excitations have been achieved in engineered metamaterials, such as structured metal surfaces and doped semiconductors [4]. Furthermore, it is noteworthy that light-matter coupling can experience significant enhancements in hyperbolic materials (HMs), which are characterized by opposing signs in the principal components of permittivity [5,6]. Electromagnetic waves traversing through HMs exhibit hyperbolic dispersion relations, enabling the propagation of highly confined surface plasmon polaritons (SPPs). These distinctive hyperbolic properties give rise to a plethora of intriguing phenomena, such as negative refraction [7,8], negative reflection [9], broadband field canalization [10,11], and topological transitions at magic angles [12]. These exotic optical scenarios offer innovative opportunities for designing advanced optical devices.

The emergence of graphene has paved the way for exciting developments in plasmon devices, owing to its excellent mechanical properties, high thermal conductivity, and exceptional carrier mobility [13–17]. Moreover, when graphene sheets are precisely patterned into micro- (nano)structures, they form atomically thin metasurfaces capable of supporting the propagation of hyperbolic SPPs [18,19]. However, graphene-based plasmon devices encounter two significant limitations: (1) The in-plane optical isotropy inherent in unpatterned graphene, stemming from its isotropic DCs, restricts its ability to provide directional guidance and support the unidirectional propagation of SPPs. Additionally, patterned graphene has a limited ceiling for the plasmon wave vector due to current constraints in nanotechnology. (2) The plasmons in charge-doped graphene are sensitive to perturbations in Fermi level, which can be induced by defects, thermal fluctuations, electric gates, or charge transfer at interfaces [20]. In light of these limitations, substantial endeavors have been dedicated to achieving resilient plasmonic behavior [20–22].

In this study, we introduce a dual anisotropic Dirac cone (DADC) model to address the two key limitations. We demonstrate that the DADC model exhibits highly anisotropic plasmons, leading to broad hyperbolic regions capable of supporting hyperbolic SPPs without the need for structural patterning. A fascinating aspect of our findings is that as the Fermi level varies between the Dirac points (DPs) of the two DCs, the plasmon frequency remains independent of Fermi level. Furthermore, we identify a unique graphene allotropy named "ω-graphene" [23] as a suitable material for this model. Through first-principles calculations, we predict that the pristine ω-graphene boasts low-loss plasmons with frequency ranging up to 1.68 eV along the x direction, reaching into the visible light spectrum, and up to 0.128 eV along the y direction. Moreover, the anisotropic response results in a low-loss hyperbolic region ($0.48 - 1.16\,\mathrm{eV}$). Impressively, the plasmon frequency remains nearly unaffected as the fluctuation amplitude of electron density within -2.89×10^{13} to 1.95×10^{13} cm^{-2} ($\pm$ corresponding to the addition or removal of electrons from the material). We also conduct simulations based on Maxwell's equations to confirm the directional propagation of hyperbolic SPPs within the

*Contact author: zmw@sdu.edu.cn

hyperbolic region. Our findings not only offer a promising candidate for plasmon applications but also provide valuable principles for designing natural hyperbolic surfaces.

II. RESULTS AND DISCUSSION

A. Plasmons in a dual anisotropic Dirac cone model

1. Plasmons in 2D materials

Under the random-phase approximation [24,25], a collective plasmon mode is determined by the zeros of the dynamical dielectric function

$$\varepsilon(\boldsymbol{q},\omega) = 1 - V(q)\Pi(\boldsymbol{q},\omega). \tag{1}$$

For a two-dimensional (2D) system, the Fourier transform of the Coulomb potential, $V(q)$ can be written as $V_{2D}(q) = 2\pi e^2/\varepsilon_r q$, with ε_r being the background dielectric constant. The intraband and interband transitions of electrons lead to the Linhard expression of polarization function (electron response function) $\Pi(\boldsymbol{q},\omega)$ [26,27] (we take $e = \hbar = 1$ hereafter),

$$\Pi(\boldsymbol{q},\omega) = \frac{g_s}{(2\pi)^2}\sum_{l,l'}\int d^2\boldsymbol{k} \times \frac{f(E_{\boldsymbol{k},l}) - f(E_{\boldsymbol{k}+\boldsymbol{q},l'})}{\omega + E_{\boldsymbol{k},l} - E_{\boldsymbol{k}+\boldsymbol{q},l'} + i\eta} F_{l,l'}(\boldsymbol{k},\boldsymbol{q}), \tag{2}$$

with $F_{l,l'}(\boldsymbol{k},\boldsymbol{q}) \equiv |\langle l,\boldsymbol{k}|e^{-i\boldsymbol{q}\cdot\boldsymbol{r}}|l',\boldsymbol{k}+\boldsymbol{q}\rangle|^2$, where g_s is the spin degeneracy, $E_{\boldsymbol{k},l}$ and $|l,\boldsymbol{k}\rangle$ represent the eigenenergy and electron wave function of the state at band l and the wave vector of $\mathbf{k}$, and $f(E)$ is the Fermi distribution function.

For intraband transitions ($l = l'$), we have $F_{l,l'}(\boldsymbol{k},\boldsymbol{q}) = \delta_{ll'}$. Consequently, polarization function resulting from intraband transitions can be written as

$$\Pi_{\text{intra}}(\boldsymbol{q},\omega) = \frac{g_s}{(2\pi)^2}\sum_{l}\int d^2\boldsymbol{k}\frac{f(E_{\boldsymbol{k},l}) - f(E_{\boldsymbol{k}+\boldsymbol{q},l})}{\omega + E_{\boldsymbol{k},l} - E_{\boldsymbol{k}+\boldsymbol{q},l} + i\eta}. \tag{3}$$

In the long-wavelength limit ($q \to 0$), this can be simplified to the following expression (setting $\eta = 0$) [22]:

$$\Pi_{\text{intra}}(\boldsymbol{q},\omega) = \frac{1}{\pi}D(\theta_q)\frac{q^2}{\omega^2}, \tag{4}$$

with the Drude weight of $D(\theta_q) = \pi\rho(\mu)\times(\langle\upsilon_x^2\rangle\cos^2\theta_q + \langle\upsilon_y^2\rangle\sin^2\theta_q)$. In this expression, $\langle\upsilon_j^2\rangle = \sum_l\int d^2\boldsymbol{k}\upsilon_j^2\delta(E_{\boldsymbol{k},l}-\mu)/\sum_l\int d^2\boldsymbol{k}\delta(E_{\boldsymbol{k},l}-\mu)$, $j = x, y$ denotes the averaged square velocity along the x- and y-direction at the Fermi level μ; $\upsilon_j = \partial E_{\boldsymbol{k},l}/\partial k_j$ represents the electron velocity along the j direction; $\rho(\mu) = \frac{g_s}{(2\pi)^2}\sum_l\int \mathrm{d}^2\boldsymbol{k}\delta(\varepsilon_{\mathbf{k},l}-\mu)$ represents the electron density of states at the Fermi level μ; and θ_q denotes the angle of wave vector $\boldsymbol{q}$ relative to the x-direction. The polarization function distinctly demonstrates its reliance on both the wave-vector direction and the electron density of states at the Fermi level.

For interband transitions ($l \neq l'$), we have $F_{l,l'}(\boldsymbol{k},\boldsymbol{q}) \approx |\langle l,\boldsymbol{k}|\boldsymbol{q}\cdot\boldsymbol{r}|l',\boldsymbol{k}+\boldsymbol{q}\rangle|^2$ in the long-wavelength limit. Without loss of generality, we considered the interband transitions between two bands, i.e., $l, l' \in (1, 2)$. The contribution of the interband transition to the polarization function can be expressed as

$$\Pi_{\text{inter}}(\boldsymbol{q},\omega) \approx \frac{g_s}{(2\pi)^2}\int d^2\boldsymbol{k}\frac{\xi(\boldsymbol{k},\theta_q)}{\omega^2 - \Omega_{12}^2}q^2, \tag{5}$$

with $\xi(\boldsymbol{k},\theta_q) = 2(f(E_{\boldsymbol{k},2}) - f(E_{\boldsymbol{k},1}))\Omega_{12}|\langle 1,\boldsymbol{k}|x\cos\theta_q + y\sin\theta_q|2,\boldsymbol{k}\rangle|^2$ and $\Omega_{12} = E_{\boldsymbol{k},2} - E_{\boldsymbol{k},1}$. Assuming Ω_{12} is independent of $\boldsymbol{k}$, the interband transition contribution can be simplified to a Lorentzian term,

$$\Pi_{\text{inter}}(\boldsymbol{q},\omega) \approx \frac{1}{\pi}\frac{S(\theta_q)}{\omega^2 - \omega_b^2}q^2, \tag{6}$$

with $S(\theta_q) \approx \frac{g_s}{4\pi}\int d^2\boldsymbol{k}\xi(\boldsymbol{k},\theta_q)$ and $\omega_b = |\Omega_{12}|$.

The total polarization function is expressed as follows:

$$\Pi(\boldsymbol{q},\omega) = \Pi_{\text{intra}}(\boldsymbol{q},\omega) + \Pi_{\text{inter}}(\boldsymbol{q},\omega) = \left(\frac{D(\theta_q)}{\omega^2} + \frac{S(\theta_q)}{\omega^2 - \omega_b^2}\right)\frac{q^2}{\pi}. \tag{7}$$

The zeros of the dynamical dielectric function [$\varepsilon(\boldsymbol{q},\omega) = 0$] yield the following dispersion relation of plasmons:

$$\omega^{\pm}(\boldsymbol{q}) = \sqrt{\left(\kappa \pm \sqrt{\kappa^2 - 2\varepsilon_r D\omega_b^2 q}\right)/\varepsilon_r} \tag{8}$$

with $\kappa = \omega_b^2\varepsilon_r/2 + q(D+S)$ and $\pm$ corresponding to the high-frequency (low-frequency) branches, respectively. Each plasmon branch contains the contributions from both intraband and interband transition, which are characterized by the Drude weight (D) and Lorentzian weight (S) within the dispersion relations. For $q \to 0$, Eq. (8) is simplified to $\omega^-(q \to 0) \approx (2Dq/\varepsilon_r)^{1/2}$ and $\omega^+(q \to 0) \approx \omega_b$, corresponding to the intraband and interband feature of plasmons, respectively. In large wave-vector limit, $q \gg \omega_b^2\varepsilon_r/2(D+S)$, the low-frequency branch attains its maximal value, $\omega_{\max}^-(\boldsymbol{q}) = \omega_b/\sqrt{1+S/D}$, while the high-frequency branch is simplified to $\omega^+(\boldsymbol{q}) \approx (2(D+S)q/\varepsilon_r)^{1/2}$. Notably, the dependence of both the Drude weight (D) and the spectral weight (S) on the direction of wave vector $\boldsymbol{q}$ demonstrates the anisotropy of plasmons.

2. Dual anisotropic Dirac cone model

We start from a 2D system with an anisotropic DC described by the Hamiltonian [28]

$$\mathcal{H}_{\text{DC}}(\boldsymbol{k}) = \begin{pmatrix} \mu_{\text{DP}} & \upsilon_x k_x - i\upsilon_y k_y \\ \upsilon_x k_x + i\upsilon_y k_y & \mu_{\text{DP}} \end{pmatrix}. \tag{9}$$

Here, k_x and k_y denote the electron wave vectors relative to the Dirac point (DP), and μ_{DP} is the energy at the DP. Both υ_x and υ_y are positive and independent of electron wave vector. The anisotropy of the DC can be described by $\beta = \upsilon_x/\upsilon_y$ with $\beta = 1$ representing an isotropic DC as the case of graphene.

For the 2D anisotropic Dirac system, we have the following relations:

$$\rho(\mu) = \frac{g_s|\mu - \mu_{\text{DP}}|}{2\pi\upsilon_x\upsilon_y}, \langle\upsilon_x^2\rangle = \frac{\upsilon_x^2}{2}, \langle\upsilon_y^2\rangle = \frac{\upsilon_y^2}{2}, \tag{10}$$

leading to

$$D(\theta_q) = \frac{g_s|\mu - \mu_{\text{DP}}|}{4}(\beta\cos^2\theta_q + \beta^{-1}\sin^2\theta_q). \tag{11}$$

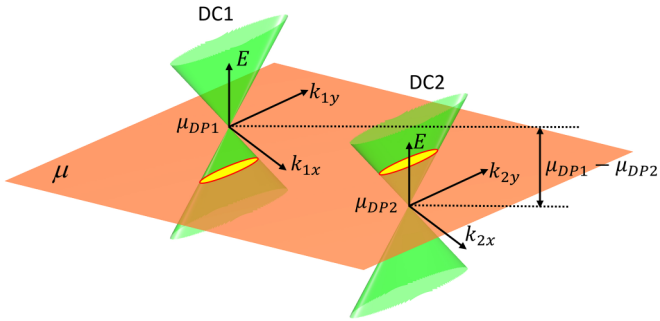

FIG. 1. Schematic representation of dual anisotropic Dirac cones model. The orange plane signifies the Fermi level's position which varies between the two Dirac points. The sections between the Dirac cones and this plane, indicated by the red ellipses, delineate the Fermi contours of the model.

Certainly, we have observed a distinctive anisotropic Drude weight, which is closely linked to the anisotropy (β) of DC. It is worth highlighting that the dependence of Drude weight (D) on the Fermi level μ demonstrates the tunability of plasmons via charge doping, akin to the behavior observed in graphene plasmons [29].

As shown in Fig. 1, we then examine a 2D Dirac system involving dual anisotropic DCs, as described by the Hamiltonian,

$$H(\boldsymbol{k}) = \begin{pmatrix} \mathcal{H}_{\mathrm{DC1}} & 0 \\ 0 & \mathcal{H}_{\mathrm{DC2}} \end{pmatrix}, \tag{12}$$

with

$$\mathcal{H}_{\mathrm{DC1}} = \begin{pmatrix} \mu_{\mathrm{DP1}} & \upsilon_{1x}k_{1x} - i\upsilon_{1y}k_{1y} \\ \upsilon_{1x}k_{1x} + i\upsilon_{1y}k_{1y} & \mu_{\mathrm{DP1}} \end{pmatrix}$$
$$\mathcal{H}_{\mathrm{DC2}} = \begin{pmatrix} \mu_{\mathrm{DP2}} & \upsilon_{2x}k_{2x} - i\upsilon_{2y}k_{2y} \\ \upsilon_{2x}k_{2x} + i\upsilon_{2y}k_{2y} & \mu_{\mathrm{DP2}} \end{pmatrix}. \tag{13}$$

In these expressions, μ_{DP1} and μ_{DP2} ($\mu_{\mathrm{DP1}} > \mu_{\mathrm{DP2}}$) represent the energies of the two DCs, respectively. The definitions of other parameters are similar to those of Eq. (9). Assuming that the separation between the two DCs in reciprocal space is significantly larger than the length of the wave vector of the plasmons, the contributions of electron transitions between the two DCs can be neglected. In such instance, the coupling between the two DCs can be omitted for the sake of simplification.

The Hamiltonian gives the electron density of states as

$$\rho(\mu) = \rho_{\mathrm{DC1}}(\mu) + \rho_{\mathrm{DC2}}(\mu)$$
$$= \frac{g_s}{2\pi\upsilon_{1x}\upsilon_{1y}}|\mu - \mu_{\mathrm{DP1}}| + \frac{g_s}{2\pi\upsilon_{2x}\upsilon_{2y}}|\mu - \mu_{\mathrm{DP2}}|. \tag{14}$$

Supposing the two DCs have the same anisotropy ($\upsilon_{1x} = \upsilon_{2x} \equiv \upsilon_x$, $\upsilon_{1y} = \upsilon_{2y} \equiv \upsilon_y$), the electron density of states within the region $\mu_{\mathrm{DP2}} < \mu < \mu_{\mathrm{DP1}}$ becomes independent of the Fermi level,

$$\rho(\mu) = \frac{g_s}{2\pi\upsilon_x\upsilon_y}(\mu_{\mathrm{DP1}} - \mu_{\mathrm{DP2}}). \tag{15}$$

This phenomenon can be elucidated by the variation in the Fermi level between the Dirac points of the two DCs, causing an increase in the electron density of states in one DC and, inevitably, a simultaneous decrease in the electron density of states in the other Dirac cone. In this case, we get

$$D(\theta_q) = \frac{g_s(\mu_{\mathrm{DP1}} - \mu_{\mathrm{DP2}})}{4}(\beta\cos^2\theta_q + \beta^{-1}\sin^2\theta_q). \tag{16}$$

Therefore, under the long-wavelength approximation $q \to 0$, the Drude weight D becomes insensitive to the Fermi level, as $\mu_{\mathrm{DP2}} < \mu < \mu_{\mathrm{DP1}}$. This feature is associated with the dual DCs, and leads to the electron density of states (ρ) and anisotropy (β) at the Fermi level being independent of the Fermi level's position. Additionally, interband transitions occurring at high energies are typically less influenced by the Fermi level's position compared to intraband transitions. We therefore assume that shifts in Fermi level between the two DPs exert a negligible influence on the Lorentzian term (S). Consequently, the plasmon dispersion described in Eq. (8) displays a behavior that is independent of the Fermi level.

3. Hyperbolicity of SPPs

The hyperbolicity of SPPs in 2D materials is featured by conductivities with opposite signs along two orthogonal directions (taken as x- and y directions) within specific frequency regions (referred to as hyperbolic regions) [11]. The relation between conductivity $\sigma(\boldsymbol{q}, \omega)$ and the polarization function in the homogeneous and local response limit, $\sigma(\boldsymbol{q}, \omega) = ie^2\Pi(\boldsymbol{q}, \omega)/q^2$ [30,31] leads to the expression of the conductivities along the x- and y directions σ_{jj} as (setting $e = 1$)

$$\sigma_{jj}(\omega) = \frac{i}{\pi}\frac{D_j}{\omega} + \frac{i}{\pi}\frac{S_j}{\omega^2 - \omega_b^2}, j = x, y, \tag{17}$$

with $D_x \equiv D(\theta_q = 0), D_y \equiv D(\theta_q = \pi/2)$, $S_x \equiv S(\theta_q = 0)$, and $S_y \equiv S(\theta_q = \pi/2)$. This expression corresponds to that of Ref. [32] without considering damping rates of both intraband and interband transitions. The hyperbolic region can be precisely located by identifying the zero point (Ω_j) with

$$\Omega_j = \frac{\omega_b}{\sqrt{1 + S_j/D_j}}, \tag{18}$$

which is highly dependent on the anisotropic electronic structured characterized by $S(\theta_q)/D(\theta_q)$. More interestingly, the zero points of conductivities equal the maximal frequencies of the low-frequency anisotropic plasmons $\omega_{\mathrm{max}}^{-}(\boldsymbol{q})$ expressed in Eq. (8). Notably, the incorporation of damping rates in Eq. (17) would lead to a slight derivation of the hyperbolic region from that predicted by Eq. (18), as illustrated in subsequent sections. Nonetheless, the straightforward relationship between the $\omega_{\mathrm{max}}^{-}(\boldsymbol{q})$ and the boundaries of the hyperbolic region offers a foundational principle for broadening this region. Specifically, enhancing the disparity between S_x/D_x and S_y/D_y can expand the hyperbolic region, which is a valuable insight for hyperbolic material engineering.

B. Anisotropic plasmons in ω-graphene monolayer

Several graphene allotropies have been predicted to showcase exceptional plasmonic properties that outperform those

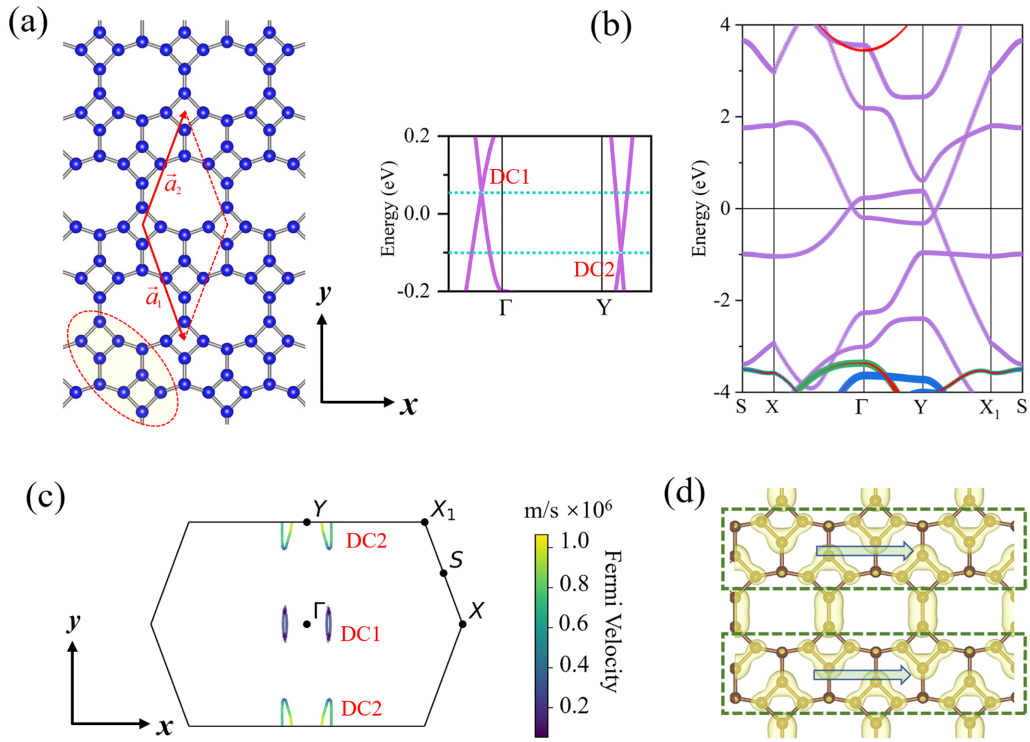

FIG. 2. Lattice and electronic structures of ω-graphene. (a) Lattice structure and (b) electronic band structure. The enlarged view near the Fermi level is presented in the left panel. The energy at the Fermi level is set to zero. (c) The Fermi contours and the corresponding Fermi velocity. (d) The isosurfaces of the charge density of the Kohn-Sham electron wave function for the states near the Fermi level. The arrows indicate the conducting channels within the compact carbon nanoribbon components.

of traditional graphene [33,34]. In this study, we have explored a 2D graphene allotropy known as ω-graphene monolayer [23] to fulfill the objectives outlined above. The involvement of rectangles and decagons in the ω-graphene enhances the structural anisotropy, highlighted by the substantial deviation of the bond angles (87°–152°) from the standard sp^2-hybridized value of 120° in graphene. A closer look reveals that this structure can be envisioned as an array of tightly packed carbon nanoribbons, comprising rhombuses and hexagons, oriented along the x direction. These nanoribbons are connected by a sparse density of covalent bonds along the y direction. This feature can also be visualized through the spatial distribution of the Kohn-Sham electron wave function of the states near the Fermi level, as depicted in Fig. 2(d). The structure parameters and the stability of ω-graphene are presented in the Supplemental Material [35]. Notably, it is interesting to observe that ω-graphene share the same structural unit, consisting of two rhombuses connected by a hexagon, as biphenylene, which has been successfully synthesized in previous studies [36]. This interesting similarity suggests a potential synthetic pathway for ω-graphene.

While the electronic bands of ω-graphene in proximity to the Fermi levels are primarily contributed by the in-plane isotropic p_z orbitals of carbon atoms, the evident anisotropy of these bands is quite pronounced, as illustrated in Fig. 2(b). Specifically, along the Γ-X direction (x direction), a band crossing occurs between the valence- and conduction bands, displaying the characteristics of a DC. Conversely, along the Γ-Y direction (y direction), there exists a gap of approximately 0.6 eV between the valence band and conduction band. Furthermore, another band crossing between the valence- and conduction bands emerges along the Y-X_1 direction. The isoenergy contours of electronic states near the Fermi level reveal the presence of two anisotropic DCs, which we shall refer to as DC1 and DC2. The anisotropic properties of the two DCs are distinctly characterized by their Fermi velocities, $v_F = (\partial E(k)/\partial k)_{k=k_F}$. For DC1, the Fermi velocity reaches 0.51×10^6 m/s along the x direction, which is markedly higher compared to 0.24×10^5 m/s in the y direction for DC1. Similarly, DC2 exhibits a pronounced anisotropy with a Fermi velocity of 0.75×10^6 m/s along the x direction, which significantly surpasses the 0.93×10^5-m/s velocity along the y direction. Notably, the DPs of the two DCs in the pristine ω-graphene monolayer (without charge doping) do not align precisely with the Fermi level; instead, they are situated 42/78 meV above/below the Fermi level for DC1/DC2, respectively. The dual DCs observed in ω-graphene meet the basic criteria outlined in our DADC model, despite certain variations in the anisotropy of the two DCs. For example, the contours of the Fermi surfaces derivate slightly from the elliptical feature of our model.

The anisotropy observed in the electronic bands stems from the anisotropic nature of the atomic arrangement. Specifically, in the x direction, the interactions of the p_z orbitals lead to the formation of densely packed π-conjugated states within the compact carbon nanoribbon components, facilitating electron motion. Conversely, in the y direction, electron motion is impeded due to the parse density of covalent bonds. These

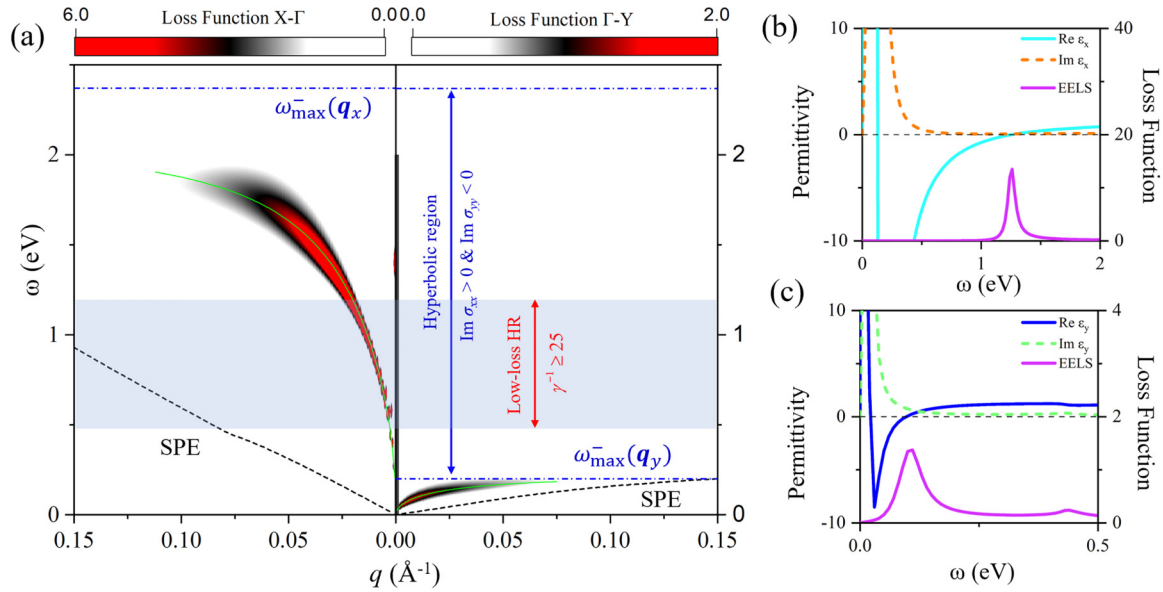

FIG. 3. Plasmonic properties of ω-graphene. (a) Electron energy-loss spectra (EELS) along the x- and y directions. The peaks of the EELS indicate the dispersion relations of plasmons. The green lines denote the fitting data given by using Eq. (8) with the maximal frequencies of $\omega^{-}_{max}(\boldsymbol{q})$ that delineate the hyperbolic region. The shadow region indicates the low-loss hyperbolic region (HR) with $\gamma^{-1} \geqslant 25$. The black dashed lines indicate the boundaries of single-particle excitation (SPE) region for intraband transitions. (b) The dielectric function along the x direction and EELS at $q_x = 0.024$ Å^{-1}. (c) The dielectric function along the y direction and EELS at $q_y = 0.012$ Å^{-1}. The red circles indicate the frequencies of low-loss plasmons.

features can also be visualized through the spatial distribution of the Kohn-Sham electron wave function of the states near the Fermi level, as depicted in Fig. 2(d). Moreover, the anisotropy of the electronic structure of ω-graphene can be confirmed from the Fermi contours, as illustrated in Fig. 2(c). In contrast to the circular Fermi contours of graphene, ω-graphene exhibits elliptical-like Fermi contours, leading to distinct electron velocities along the x- and y directions. The Fermi velocity can reach up to $\sim 10^6$ m/s, which is comparable to that in graphene.

We then calculated the dynamical dielectric function of pristine ω graphene using Eqs. (1) and (2) and the electron energy-loss spectrum (EELS) defined as $L(\mathbf{q}, \omega) = -\mathrm{Im}[1/\varepsilon(\mathbf{q}, \omega)]$. Both $E_{\boldsymbol{k},l}$ and $|l, \boldsymbol{k}\rangle$ are precisely generated through first-principles calculations. The EELS in the region of 0–2 eV along the x- and the y directions are plotted in Fig. 3(a). By extracting the local peaks of EELS, we obtained distinct dispersions along the two directions. In the x direction, we observed the low-loss plasmons with frequencies reaching up to 1.68 eV, extending into the visible light regimes. This extensive frequency range can be attributed to the high electron velocity along this direction. Conversely, along the y direction, the low-loss plasmon frequency is confined to a range up to 0.128 eV. This disparity in plasmon behavior between the x- and y directions highlights the significant anisotropy of plasmons in ω-graphene monolayer. This observation aligns with the anisotropic plasmon dispersions expressed by Eq. (8), where the dependence of both the Drude weight (D) and the spectral weight (S) on the direction of wave vector $\boldsymbol{q}$ shows anisotropy.

The presence of low-loss plasmons is further confirmed through the analysis of the dielectric function $\varepsilon(\mathbf{q}, \omega)$ calculated using Eqs. (1) and (2) at $q_x = 0.024$ Å^{-1} and $q_y = 0.012$ Å^{-1}, as illustrated in Fig. 3(b) and Fig. 3(c). Specially, the real parts of dielectric function (Reε) exhibit zero-crossing points that align with the peaks observed in EELS data. To classify a collective excitation as a nearly undamped plasmon at a given energy, it is imperative that the dielectric function satisfies $\mathrm{Re}\varepsilon = 0$ while $\partial \mathrm{Re}\varepsilon/\partial\omega > 0$ at the peak of the loss function. When Im(ε) approaches zero at this energy, it signifies a nearly undamped plasmonic mode [29]. At $q_x = 0.024$ Å^{-1} and $q_y = 0.012$ Å^{-1}, the condition $\mathrm{Im}\varepsilon \to 0$ is met at zero-crossing points corresponding to the frequency of 1.26 and 0.095 eV in the real parts of permittivities, unequivocally indicating the presence of nearly undamped plasmonic modes.

The anisotropic plasmon dispersions along the x- and y directions can be fitted using the low-frequency branch of Eq. (8). The fitting data are represented by the green lines, as shown in Fig. 3(a), with the fitting parameters of $D_x = 42$ eV^2 Å, $S_x = 28$ eV^2 Å, and $\omega_b = 2.75$ eV for the x direction, and $D_y = 0.5$ eV^2 Å, $S_y = 81$ eV^2 Å, and $\omega_b = 2.75$ eV for the y direction. The high-frequency branch is damped and thus absent in the EELS. It is noteworthy that as the frequency approaches the edges of the hyperbolic region, there is a substantial increase in plasmon damping, which can be attributed to the enhanced interband transitions.

We proceeded to assess the stability of anisotropic plasmons in ω-graphene in response to the fluctuation of the Fermi level (equivalently electron density). We varied the Fermi level in the range of $-/+ 50$ meV relative to that of the pristine ω-graphene, by removing or adding electrons to ω-graphene. This range corresponds to an electron density-fluctuation amplitude spanning from -2.89×10^{13} to 1.95×10^{13} cm^{-2},

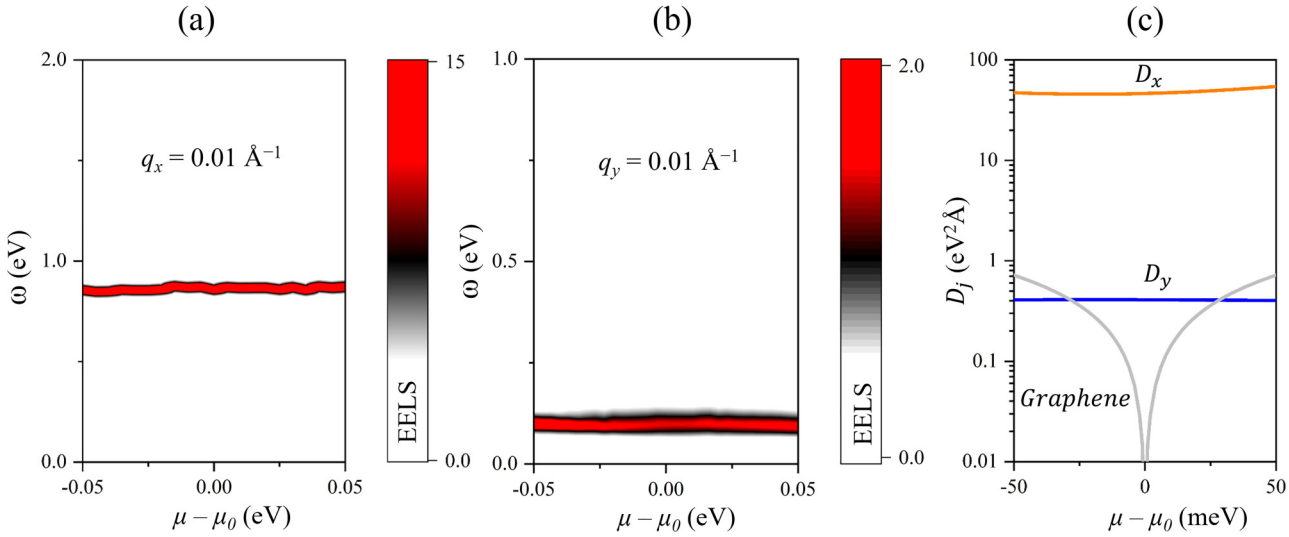

FIG. 4. Plasmonic properties of charge-doped ω-graphene. (a), (b) the EELS as a function of frequency (ω) and Fermi energy (μ) relative to that (μ_0) of pristine ω-graphene at $q_x = 0.01$ Å^{-1} and $q_y = 0.01$ Å^{-1}, respectively. (c) The variation of Drude weight (D) along the Γ-X and Γ-Y direction of charge-doped ω-graphene as a function of energy relative to the Fermi level is shown by orange and blue lines, respectively. The Drude weight (D) of graphene as a function of Fermi energy is depicted by the gray lines.

which is comparable to the highest order of magnitude of experimentally realized doping concentrations via different approaches [37–41]. The EELSs along the x- and y direction at wave vector $q_x = q_y = 0.01$ Å^{-1} within this range of Fermi level are plotted in Figs. 4(a) and 4(b). The plasmonic dispersions of the charge-doped ω-graphene monolayers are presented in the Supplemental Material [35]. Remarkably, the plasmon frequency demonstrates robustness, exhibiting fluctuation of less than 5% (along the x direction) and 2% (along the y direction). The Drude weights D_x and D_y, as a function of Fermi level, depicted in Fig. 4(c), also confirm the robustness of the plasmon frequency in ω-graphene against Fermi-level variations.

We should stress that the electronic band structure of ω-graphene does not entirely conform to the requirements outlined in our DADC model. Specifically, the two DCs in ω-graphene exhibit distinct anisotropy, leading to small fluctuation in plasmons frequency as the Fermi level varies between the two Dirac points. Additionally, the Dirac cone approximation is effective only within a limited energy region of ∼0.3 eV, making it unsuitable for describing the high-frequency plasmons observed in first-principles calculations. Our DADC model, however, presents a promising strategy for stabilizing plasmon frequency against variations in the Fermi level. This strategy based on the observation that changes in the Fermi energy, resulting in an increase in carrier density in one Dirac cone, inevitably leads to a decrease in carrier density in the other Dirac cone simultaneously. The high-frequency plasmons in ω-graphene unveiled from first-principles calculations are primarily driven by the electron transitions between the two flatbands along the S-X and $X1$-S directions, which surpasses the capability of the DADC model. These transitions can be represented by a Lorentz term with $\omega_b = 2.75$ eV. Nevertheless, the synthesis of ω-graphene would offer an enticing avenue for the development of a 2D material capable of sustaining robust anisotropic plasmons against fluctuations of electron density caused by external disturbances and internal inhomogeneities.

C. Directional SPPs on ω-graphene monolayer

The directional propagation behaviors of SPPs on 2D materials can be simulated using a complete electromagnetic approach based on Maxwell's electromagnetic field theory [22,33,34,42,43]. SPPs emerge from the coupling between the intrinsic plasmons and the electromagnetic field of the incident light. When considering the eigenmodes confined within the ω-graphene monolayer (x-y plane) characterized by $e^{i(q_x x+q_y y)}e^{-pz}$ (for $z > 0$) and $e^{i(q_x x+q_y y)}e^{pz}$ for ($z < 0$), we can derive the dispersion relations of the SPPs as [42]

$$\left(q_x^2 - k_0^2\right)\sigma_{xx} + \left(q_y^2 - k_0^2\right)\sigma_{yy} = 2ip\omega\left(\varepsilon_0 + \frac{\mu_0\sigma_{xx}\sigma_{yy}}{4}\right). \tag{19}$$

Here, ε_0, μ_0, and $k_0 = \omega\sqrt{\varepsilon_0\mu_0}$ represent the permittivity, permeability, and wave number in vacuum, $p = \sqrt{q_x^2 + q_y^2 - k_0^2}$. For $\mathrm{Im}\sigma \gg \mathrm{Re}\sigma$, Eq.(19) reduces to

$$\left(\tilde{q}_x^2 - 1\right) + \zeta\left(\tilde{q}_y^2 - 1\right) = \kappa\left(\tilde{q}_x^2 + \tilde{q}_y^2 - 1\right)^{1/2}, \tag{20}$$

with $\tilde{q}_x = q_x/k_0$, and $\tilde{q}_y = q_y/k_0$. The values of ζ and κ are derived from the optical conductivities of ω-graphene monolayer:$\zeta = \mathrm{Im}\sigma_{yy}/\mathrm{Im}\sigma_{xx}$ and $\kappa = (2\varepsilon_0/(\mu_0\mathrm{Im}\sigma_{xx} \times \mathrm{Im}\sigma_{yy}) - 1/2)\mathrm{Im}\sigma_{yy}(\varepsilon_0/\mu_0)^{-1/2}$. For $\zeta < 0$, Eq. (20) exhibits two asymptotic lines given by $q_x^2 + \zeta q_y^2 = 0$ for $\tilde{q}_x \gg 1$ and $\tilde{q}_y \gg 1$. This observation implies that the direction of propagation for SPPs beams, which is determined by the group velocity normal to the contour line, can be characterized by an angle of $\varphi = \pm\tan^{-1}|\zeta|^{1/2}$ relative to the x direction.

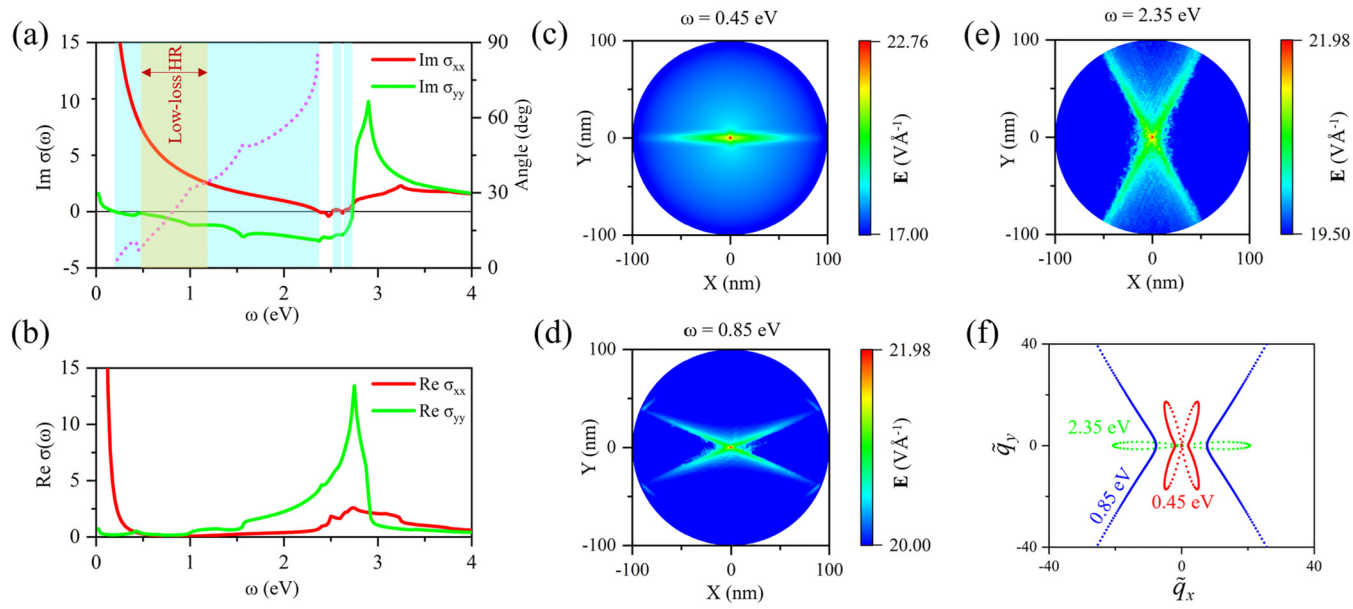

FIG. 5. Hyperbolicity and SPPs in ω-graphene. (a) Imaginary and (b) real parts of the conductivity of ω-graphene. The hyperbolic regimes with $\mathrm{Im}\sigma_{xx} > 0$, $\mathrm{Im}\sigma_{yy} < 0$ are indicated by the shadow areas. The low-loss hyperbolic region (HR) is determined by $\gamma^{-1} \geqslant 25$. The angle of the surface plasmons relative to the x direction is plotted by the purple dotted line. The spatial distribution of the electric field of the surface plasmons on ω-graphene at (c) $\omega = 0.45$ eV, (d) $\omega = 0.85$ eV, and (e) $\omega = 2.35$ eV. (f) The topologies of the isofrequency contours at the three selected frequencies.

We calculated the on-diagonal elements of conductivity $\sigma_{jj}(\omega)$, $j = x, y$ using the expression [41,44,45]

$$\sigma_{jj}(\omega) = \frac{i}{(\omega + i\eta)} \sum_{\boldsymbol{k},l} \left(\frac{\partial E_{\boldsymbol{k},l}}{\partial \boldsymbol{k}_j}\right)^2 \left(-\frac{\partial f(E_{\boldsymbol{k},l})}{\partial E_{\boldsymbol{k},l}}\right) + i \sum_{\boldsymbol{k},l\neq l'} \frac{f(E_{\boldsymbol{k},l'}) - f(E_{\boldsymbol{k},l})}{(E_{\boldsymbol{k},l'} - E_{\boldsymbol{k},l}) - (\omega + i\eta)} \times \frac{1}{E_{\boldsymbol{k},l'} - E_{\boldsymbol{k},l}} |\langle l, \boldsymbol{k}|\hat{v}_j|l', \boldsymbol{k}\rangle|^2. \quad (21)$$

In this expression, $\hat{v}_j$ represents the velocity operator along the j direction, with other symbols defined in the same manner as in Eq. (2). The two terms represent the contributions from intraband and interband transitions, respectively. The imaginary and real parts of the conductivity of ω-graphene are shown in Fig. 5(a) and 5(b). There is a board region of $\mathrm{Im}\sigma_{xx} > 0$, $\mathrm{Im}\sigma_{yy} < 0$ spanning from 0.20 to 2.37 eV, which can be correlated to the significantly anisotropic plasmons along the x- and y directions.

The real component of conductivity ($\mathrm{Re}\sigma$) signifies the energy loss. A substantial energy loss, as indicated by an elevated $\mathrm{Re}\sigma$ value, leads to a diminished propagation distance for plasmons. Therefore, for the practical implementation of hyperbolic behaviors, it is essential to minimize the $\mathrm{Re}\sigma$ value within hyperbolic regions. As depicted in Fig. 5(b), one can find ω-graphene has low energy loss within the energy range of $0.5 - 1.5$ eV, but experiences significant energy dissipation between 1.5 and 2.37 eV. The effect of energy loss on plasmonic properties can be quantified by the figures of merit, $\gamma = \mathrm{Im}\,\boldsymbol{q}/\mathrm{Re}\,\boldsymbol{q}$, as proposed in prior studies [46]. The inverse of γ ($\gamma^{-1}/2\pi$) reflects the number of oscillation cycles that SPPs can sustain before their amplitude diminishes by a factor of $1/e$. Previous research has shown that hBN-encapsulated graphene can reach a γ^{-1} value of approximately 25 [47], while unencapsulated graphene on a silicon dioxide substrate achieves a lower γ^{-1} value of around 5 [48,49]. The γ^{-1} values of ω-graphene obtained from our calculations are plotted in Fig. S4 in the Supplemental Material [35]. Notably, within the energy region of 0.48–1.16 eV, ω-graphene demonstrates $\gamma^{-1} > 25$, reaching a peak value of approximately 50 at 0.88 eV, surpassing that of hBN-encapsulated graphene [47]. This specific range is hence referred to as low-loss hyperbolic region of ω-graphene, as denoted in Fig. 3(a) and Fig. 5(a).

To further visualize this fascinating scenario, we conducted numerical simulations of the propagation of SPPs on the ω-graphene surface, based on Maxwell's equations. We considered a single layer of ω-graphene with a radius of 100 nm and a thickness of 1 nm surrounded by a vacuum. A z-direction polarized dipole is placed 1 nm above the sheet to excite the surface wave. We numerically solved Maxwell's equations for the system using a commercial finite-difference time-domain method from COMSOL [50]. This approach allowed us to determine the dispersion relation and spatial distribution of the surface plasma electric field. We selected three frequencies $\omega = 0.45$, $\omega = 0.85$, and $\omega = 2.35$ eV. The conductivities of the ω-graphene sheet adopted in these simulations are obtained from the first-principles calculations. The spatial distribution of the electric field on the sheet confirms the directional propagation characteristic of the SPPs in ω-graphene, as the energy of the SPPs is directed into narrow beams, as illustrated in Figs. 5(c)–5(e). For $\omega = 0.85$ and $\omega = 2.35$ eV, the beams exhibit angles of $2\varphi = 47.76^\circ$ and 156.61° between them, respectively, consistent with Eq. (19). Remarkably, we have observed a pronounced directional propagation

of SPPs at a frequency of 0.45 eV, as illustrated in Fig. 5(c). This remarkable phenomenon can be attributed to the ultrahigh anisotropy of the conductivities, with the conductivity along the x direction being nearly two orders of magnitude larger than that along the y direction, resulting in $\varphi \approx 0^\circ$. The isofrequency contours of the SPPs corresponding to these three frequencies are depicted in Fig. 5(f), displaying hyperbolic characteristics. These results confirm that ω-graphene has the potential to guide anisotropic plasmons, highlighting their potential applications in nanophotonics and plasmonics.

III. CONCLUSIONS

In summary, the dual anisotropic Dirac cone (DADC) model proposed in this study addresses the two key limitations of graphene plasmons. First, the DADC exhibits highly anisotropic plasmons along the x- and y directions, leading to broad hyperbolic regions that facilitate the support of hyperbolic surface plasmon polaritons, eliminating the need for intricate structural patterning treatments. Second, the plasmon frequency predicted by the DADC model remains unaffected by the Fermi level, as the Fermi level fluctuates between the Dirac points of the two DCs. This robust characteristic makes it resilient to perturbation in electron density in complex environments.

Based on first-principles calculations, our study identifies ω-graphene as a potential material for the DADC model. Our computations demonstrate that ω-graphene exhibits significantly anisotropic plasmons, with a maximal frequency of 1.68 eV along the x direction and 0.128 eV along the y direction, accompanied by a low-loss hyperbolic region spanning from 0.48 to 1.16 eV. Furthermore, the plasmon frequency remains insensitive to fluctuation in electron density, ranging from -2.89×10^{13} to 1.95×10^{13} cm^{-2}. This manifests the robustness of plasmons in ω-graphene to external disturbances such as temperature, thermal perturbations, electrical bias, as well as internal defects and charge inhomogeneities. Our numerical simulations, based on Maxwell's equations, confirm that ω-graphene is capable of supporting the directional propagation of hyperbolic SPPs in the hyperbolic range. These findings open up exciting possibilities in the field of advanced optics and offer a promising strategy for designing natural hyperbolic surfaces.

ACKNOWLEDGMENTS

This study is supported by the National Natural Science Foundation of China (Grant No. 12074218) and the Taishan Scholar Program of Shandong Province (Grant No. ts20190906).

APPENDIX: METHOD AND COMPUTATIONAL DETAILS

Our first-principles calculations are performed using the Vienna *Ab initio* simulation package (VASP) [51]. The ion-electron interaction is described by the projector augmented-wave method [52] with an energy cutoff of 500 eV. The exchange-correlation function is treated self-consistently with a generalized gradient approximation (GGA) in the form of Perdew-Burke-Ernzerhof [53]. A vacuum space with 20-Å thickness is applied along the z direction to exclude the interaction between neighboring images. A $12 \times 10 \times 1$ k-point mesh was employed to sample the Brillouin zone during the structure relaxation and electronic property calculations. The lattice constants and atomic positions are fully relaxed until the atomic force on the atoms is less than 0.01 eV/Å and the total energy change is less than 10^{-5} eV. In the calculations of both dynamical dielectric function and conductivity, we considered ten bands around the Fermi level. A dense k-point grid of 1000×1000 was employed to sample the Brillouin zone. The broadening parameter was set to $\eta = 0.05$ eV.

[1] A. H. Dorrah and F. Capasso, Tunable structured light with flat optics, Science **376**, 367 (2022).
[2] N. Yu and F. Capasso, Flat optics with designer metasurfaces, Nat. Mater. **13**, 139 (2014).
[3] Y. Jin, Y. Pennec, B. Bonello, H. Honarvar, L. Dobrzynski, B. Djafari-Rouhani, and M. I. Hussein, Physics of surface vibrational resonances: Pillared phononic crystals, metamaterials, and metasurfaces, Rep. Prog. Phys. **84**, 086502 (2021).
[4] F. J. Garcia-Vidal, A. I. Fernández-Domínguez, L. Martin-Moreno, H. C. Zhang, W. Tang, R. Peng, and T. J. Cui, Spoof surface plasmon photonics, Rev. Mod. Phys. **94**, 025004 (2022).
[5] A. Poddubny, I. Iorsh, P. Belov, and Y. Kivshar, Hyperbolic metamaterials, Nat. Photonics **7**, 948 (2013).
[6] L. Ferrari, C. Wu, D. Lepage, X. Zhang, and Z. Liu, Hyperbolic metamaterials and their applications, Prog. Quant. Electron. **40**, 1 (2015).
[7] Y. Liu, C. Ouyang, Q. Xu, X. Su, J. Ma, J. Zhao, Y. Li, Z. Tian, J. Gu, L. Liu, J. Han, and W. Zhang, Negative refraction in twisted hyperbolic metasurfaces, Nanophotonics **11**, 1977 (2022).
[8] H. Hu, N. Chen, H. Teng, R. Yu, M. Xue, K. Chen, Y. Xiao, Y. Qu, D. Hu, and J. Chen, Gate-tunable negative refraction of mid-infrared polaritons, Science **379**, 558 (2023).
[9] T. Zhang, C. Zheng, Z. N. Chen, and C.-W. Qiu, Negative reflection and negative refraction in biaxial van der Waals materials, Nano Lett. **22**, 5607 (2022).
[10] J. S. Gomez-Diaz, M. Tymchenko, and A. Alù, Hyperbolic plasmons and topological transitions over uniaxial metasurfaces, Phys. Rev. Lett. **114**, 233901 (2015).
[11] A. Nemilentsau, T. Low, and G. Hanson, Anisotropic 2D materials for tunable hyperbolic plasmonics, Phys. Rev. Lett. **116**, 066804 (2016).
[12] G. Hu, A. Krasnok, Y. Mazor, C.-W. Qiu, and A. Alù, Moiré hyperbolic metasurfaces, Nano Lett. **20**, 3217 (2020).
[13] F. D'Apuzzo, A. R. Piacenti, F. Giorgianni, M. Autore, M. C. Guidi, A. Marcelli, U. Schade, Y. Ito, M. Chen, and S. Lupi, Terahertz and mid-infrared plasmons in three-dimensional nanoporous graphene, Nat. Commun. **8**, 14885 (2017).
[14] X. He, Tunable terahertz graphene metamaterials, Carbon **82**, 229 (2015).

[15] Q. Li, Z. Tian, X. Zhang, R. Singh, L. Du, J. Gu, J. Han, and W. Zhang, Active graphene–silicon hybrid diode for terahertz waves, Nat. Commun. **6**, 7082 (2015).

[16] C. N. Santos, F. Joucken, D. De Sousa Meneses, P. Echegut, J. Campos-Delgado, P. Louette, J. P. Raskin, and B. Hackens, Terahertz and mid-infrared reflectance of epitaxial graphene, Sci. Rep. **6**, 24301 (2016).

[17] T. Low and P. Avouris, Graphene plasmonics for terahertz to mid-infrared applications, ACS Nano **8**, 1086 (2014).

[18] Y. Fan, N. H. Shen, F. Zhang, Q. Zhao, H. Wu, Q. Fu, Z. Wei, H. Li, and C. M. Soukoulis, Graphene plasmonics: A platform for 2D optics, Adv. Opt. Mater. **7**, 1800537 (2019).

[19] Y. Fan, N. H. Shen, T. Koschny, and C. M. Soukoulis, Tunable terahertz meta-surface with graphene cut-wires, ACS Photonics **2**, 151 (2015).

[20] J. Wang, X. Sui, W. Duan, F. Liu, and B. Huang, Density-independent plasmons for terahertz-stable topological metamaterials, Proc. Natl. Acad. Sci. USA **118**, e2023029118 (2021).

[21] C. Ding, H. Gao, W. Geng, and M. Zhao, Anomalous plasmons in a two-dimensional Dirac nodal-line Lieb lattice, Nanoscale Adv. **3**, 1127 (2021).

[22] H. Gao, X. Zhang, C. Ding, X. Ma, M. Wang, Y. Li, and M. Zhao, Highly directional and carrier density-independent plasmons in quasi-one-dimensional electron gas systems, Commun. Phys. **6**, 342 (2023).

[23] Y. Gao, Y. Liu, and D. Li, ω-Graphene: A graphene allotrope with desirable auxeticity and Dirac cone, Adv. Theor. Simul. **6**, 2300059 (2023).

[24] G. Giuliani and G. Vignale, *Quantum Theory of the Electron Liquid* (Cambridge University Press, Cambridge, 2008).

[25] S. Das Sarma and E. H. Hwang, Collective modes of the massless Dirac plasma, Phys. Rev. Lett. **102**, 206412 (2009).

[26] S. L. Adler, Quantum theory of the dielectric constant in real solids, Phys. Rev. **126**, 413 (1962).

[27] N. Wiser, Dielectric constant with local field effects included, Phys. Rev. **129**, 62 (1963).

[28] R. Fan, L. Sun, X. Shao, Y. Li, and M. Zhao, Two-dimensional Dirac materials: Tight-binding lattice models and material candidates, ChemPhysMater **2**, 30 (2023).

[29] E. H. Hwang and S. Das Sarma, Dielectric function, screening, and plasmons in two-dimensional graphene, Phys. Rev. B **75**, 205418 (2007).

[30] P. A. D. Goncalves and N. M. R. Peres, *An Introduction to Graphene Plasmonics* (World Scientific, Singapore, 2016).

[31] C. Wang, S. Huang, Q. Xing, Y. Xie, C. Song, F. Wang, and H. Yan, van der Waals thin films of WTe_2 for natural hyperbolic plasmonic surfaces, Nat. Commun. **11**, 1158 (2020).

[32] D. N. Basov, M. M. Fogler, and F. J. Garcia de Abajo, Polaritons in van der Waals materials, Science **354**, aag1992 (2016).

[33] M. Wang, H. Gao, C. Ding, X. Zhang, S. Hou, L. Sun, X. Ma, Y. Li, and M. Zhao, Hyperbolic plasmons on natural biphenylene surface, Carbon **213**, 118307 (2023).

[34] M. Dehdast, Z. Valiollahi, M. Neek-Amal, B. Van Duppen, F. M. Peeters, and M. Pourfath, Tunable natural terahertz and mid-infrared hyperbolic plasmons in carbon phosphide, Carbon **178**, 625 (2021).

[35] See Supplemental Material at http://link.aps.org/supplemental/10.1103/PhysRevB.110.085415 for lattice structures, stability, plasmonic dispersions, and damping ratio of ω-graphene. It also contains Refs. [54–57].

[36] Q. Fan, L. Yan, M. Tripp, O. Krejcí, S. Dimosthenous, S. Kachel, M. Chen, A. S. Foster, U. Koert, P. Liljeroth, and J. M. Gottfried, Biphenylene network: A nonbenzenoid carbon allotrope, Science **372**, 852 (2021).

[37] K. S. Novoselov, A. K. Geim, S. V. Morozov, D. Jiang, Y. Zhang, S. V. Dubonos, I. V. Grigorieva, and A. A. Firsov, Electric field effect in atomically thin carbon films, Science **306**, 666 (2004).

[38] F. J. García de Abajo, Graphene plasmonics: Challenges and opportunities, ACS Photonics **1**, 135 (2014).

[39] J. C. Johannsen, S. Ulstrup, A. Crepaldi, F. Cilento, M. Zacchigna, J. A. Miwa, C. Cacho, R. T. Chapman, E. Springate, F. Fromm, C. Raidel, T. Seyller, P. D. King, F. Parmigiani, M. Grioni, and P. Hofmann, Tunable carrier multiplication and cooling in graphene, Nano Lett. **15**, 326 (2015).

[40] H. Lee, K. Paeng, and I. S. Kim, A review of doping modulation in graphene, Synth. Met. **244**, 36 (2018).

[41] V. P. Gusynin, S. G. Sharapov, and J. P. Carbotte, Unusual microwave response of Dirac quasiparticles in graphene, Phys. Rev. Lett. **96**, 256802 (2006).

[42] S. A. Mikhailov and K. Ziegler, New electromagnetic mode in graphene, Phys. Rev. Lett. **99**, 016803 (2007).

[43] X. Ma, S. Hou, M. Wang, Y. Du, C. Ding, H. Gao, L. Sun, and M. Zhao, Tunable in-plane bihyperbolicity in bismuth monolayer, Phys. Rev. B **109**, 195401 (2024).

[44] V. Despoja, D. Novko, K. Dekanić, M. Šunjić, and L. Marušić, Two-dimensional and π plasmon spectra in pristine and doped graphene, Phys. Rev. B **87**, 075447 (2013).

[45] L. A. Falkovsky and A. A. Varlamov, Space-time dispersion of graphene conductivity, Eur. Phys. J. B **56**, 281 (2007).

[46] T. Low, A. Chaves, J. D. Caldwell, A. Kumar, N. X. Fang, Phaedon Avouris, T. F. Heinz, F. Guinea, L. Martin-Moreno, and F. Koppens, Polaritons in layered two-dimensional materials, Nat. Mater. **16**, 182 (2017).

[47] A. Woessner, M. B. Lundeberg, Y. Gao, A. Principi, P. Alonso-Gonzalez, M. Carrega, K. Watanabe, T. Taniguchi, G. Vignale, M. Polini, J. Hone, R. Hillenbrand, and F. H. L. Koppens, Highly confined low-loss plasmons in graphene–boron nitride heterostructures, Nat. Mater. **14**, 421 (2015).

[48] Z. Fei, A. S. Rodin, G. O. Andreev, W. Bao, A. S. McLeod, M. Wagner, L. M. Zhang, Z. Zhao, M. Thiemens, G. Dominguez, M. M. Fogler, A. H. Castro Neto, C. N. Lau, F. Keilmann, and D. N. Basov, Gate-tuning of graphene plasmons revealed by infrared nano-imaging, Nature (London) **487**, 82 (2012).

[49] J. Chen, M. Badioli, P. Alonso-González, S. Thongrattanasiri, F. Huth, J. Osmond, M. Spasenović, A. Centeno, A. Pesquera, P. Godignon, A. Z. Elorza, N. Camara, F. Javier García de Abajo, R. Hillenbrand, and F. H. L. Koppens, Optical nano-imaging of gate-tunable graphene plasmons, Nature (London) **487**, 77 (2012).

[50] www.comsol.com.

[51] G. Kresse and J. Furthmüller, Efficient iterative schemes for *ab initio* total-energy calculations using a plane-wave basis set, Phys. Rev. B **54**, 11169 (1996).

[52] P. E. Blöchl, Projector augmented-wave method, Phys. Rev. B **50**, 17953 (1994).

[53] J. P. Perdew, K. Burke, and M. Ernzerhof, Generalized gradient approximation made simple, Phys. Rev. Lett. **77**, 3865 (1996).

[54] G. Li, Y. Li, H. Liu, Y. Guo, Y. Li, and D. Zhu, Architecture of graphdiyne nanoscale films, Chem. Commun. **46**, 3256 (2010).

[55] A. W. H. Prinzbach, P. Landenberger, F. Wahl, J. Wörth, L. T. Scott, M. Gelmont, D. Olevano, and B. v. Issendorff, Gas-phase production and photoelectron spectroscopy of the smallest fullerene, C_{20}, Nature (London) **407**, 60 (2000).

[56] X. Zhao, Y. Liu, S. Inoue, T. Suzuki, R. O. Jones, and Y. Ando, Smallest carbon nanotube is 3 Å in diameter, Phys. Rev. Lett. **92**, 125502 (2004).

[57] Q. Peng, W. Ji, and S. De, Mechanical properties of graphyne monolayers: A first-principles study, Phys. Chem. Chem. Phys. **14**, 13385 (2012).